PHYSICS

Strong suppression of heat conduction in a laboratory replica of galaxy-cluster turbulent plasmas

Jena Meinecke[1], Petros Tzeferacos[1,2,3,4], James S. Ross[5], Archie F. A. Bott[1,6], Scott Feister[2,7], Hye-Sook Park[5], Anthony R. Bell[1,8], Roger Blandford[9], Richard L. Berger[5], Robert Bingham[8,10], Alexis Casner[11], Laura E. Chen[1], John Foster[12], Dustin H. Froula[4], Clement Goyon[5], Daniel Kalantar[5], Michel Koenig[13], Brandon Lahmann[14], Chikang Li[14], Yingchao Lu[3], Charlotte A. J. Palmer[1,15], Richard D. Petrasso[14], Hannah Poole[1], Bruce Remington[5], Brian Reville[16], Adam Reyes[3], Alexandra Rigby[1], Dongsu Ryu[17], George Swadling[5], Alex Zylstra[5,18], Francesco Miniati[1], Subir Sarkar[1], Alexander A. Schekochihin[1,19,20], Donald Q. Lamb[2], Gianluca Gregori[1,2]*

Copyright © 2022 The Authors, some rights reserved; exclusive licensee American Association for the Advancement of Science. No claim to original U.S. Government Works. Distributed under a Creative Commons Attribution NonCommercial License 4.0 (CC BY-NC).

In conventional gases and plasmas, it is known that heat fluxes are proportional to temperature gradients, with collisions between particles mediating energy flow from hotter to colder regions and the coefficient of thermal conduction given by Spitzer's theory. However, this theory breaks down in magnetized, turbulent, weakly collisional plasmas, although modifications are difficult to predict from first principles due to the complex, multiscale nature of the problem. Understanding heat transport is important in astrophysical plasmas such as those in galaxy clusters, where observed temperature profiles are explicable only in the presence of a strong suppression of heat conduction compared to Spitzer's theory. To address this problem, we have created a replica of such a system in a laser laboratory experiment. Our data show a reduction of heat transport by two orders of magnitude or more, leading to large temperature variations on small spatial scales (as is seen in cluster plasmas).

INTRODUCTION

Galaxy clusters are filled with hot, diffuse x-ray emitting plasma, with a stochastically tangled magnetic field whose energy is close to equipartition with the energy of the turbulent motions (*1*, *2*). In the cluster cores, the temperatures remain anomalously high compared to what might be expected considering that the radiative cooling time is short relative to the Hubble time (*3*, *4*). While feedback from the central active galactic nuclei (AGN) (*5*–*7*) is believed to provide most of the heating, there has been a long debate as to whether conduction of heat from the bulk to the core can help the core to reach the observed temperatures (*8*–*10*), given the presence of tangled magnetic fields. Evidence of very sharp temperature gradients in structures like cold fronts implies a high degree of suppression of thermal conduction (*11*).

There are a number of possible mechanisms that can lead to a reduction from the classical (local) Spitzer conductivity: electrons getting stuck in local magnetic mirrors (*12*), alignment of local temperature gradients perpendicular to magnetic fields (*13*), and plasma instabilities such as whistler waves (*14*, *15*). For these processes to occur, the electron's Larmor radius must be small compared to its Coulomb mean free path, enabling microscale changes in the electron heat transport to alter the global properties of the plasma dynamics. Numerical simulations are unable to address these issues fully (*16*, *17*), as comprehensive modeling of all the physical processes present at different scales remains very challenging computationally. Laboratory experiments (*18*) can provide an alternative approach if they can achieve sufficiently weakly collisional conditions and sufficiently strong stochastic magnetic fields for the heat transport to be substantially modified.

Here we report such an experiment using the National Ignition Facility (NIF) laser at the Lawrence Livermore National Laboratory—see Fig. 1 for details of the experimental setup. The platform is similar to that already used at other laser facilities [e.g., the Omega laser (*19*, *20*)] but with ~30 times more energy delivered to the target. A highly turbulent plasma was created by ablating two doped plastic foils, each with 133 kJ of 351 nm light in 15 ns (see Fig. 1). The foils were separated by 8 mm and ablated on the back side to create colliding plasma flows at the center (4 mm from each target). To help excite turbulence, plastic mesh grids with 300-μm apertures and 300-μm-diameter wires were placed 2 mm from each foil to disturb the two flows before they collided. Three-dimensional simulations carried out with the FLASH code [validated on previous experiments at smaller laser facilities (*20*, *21*)] were used to help design the platform and analyze the experimental data.

RESULTS

Several complementary plasma diagnostics were deployed (see Materials and Methods). With optical Thomson scattering (OTS), we measured an average electron density $n_e \approx 5 \times 10^{20}$ cm^{-3} in the collision region at $t = 25$ ns after the start of the drive beams. The

[1]Department of Physics, University of Oxford, Parks Road, Oxford OX1 3PU, UK. [2]Department of Astronomy and Astrophysics, University of Chicago, 5640 S. Ellis Ave., Chicago, IL 60637, USA. [3]Flash Center for Computational Science, Department of Physics and Astronomy, University of Rochester, 206 Bausch & Lomb Hall, Rochester, NY 14627, USA. [4]Laboratory for Laser Energetics, University of Rochester, 250 E. River Rd., Rochester, NY 14623, USA. [5]Lawrence Livermore National Laboratory, Livermore, CA 94550, USA. [6]Department of Astrophysical Sciences, Princeton University, 4 Ivy Ln, Princeton, NJ 08544, USA. [7]Department of Computer Science, California State University Channel Islands, 1 University Dr, Camarillo, CA 93012, USA. [8]Rutherford Appleton Laboratory, Chilton, Didcot OX11 0QX, UK. [9]Department of Physics, Stanford University, Stanford, CA 94309, USA. [10]Department of Physics, University of Strathclyde, Glasgow G4 0NG, UK. [11]CEA, DAM, DIF, 91297 Arpajon, France. [12]AWE, Aldermaston, Reading, West Berkshire RG7 4PR, UK. [13]Laboratoire pour l'Utilisation de Lasers Intenses, UMR7605, CNRS CEA, Universitè Paris VI Ecole Polytechnique, 91128 Palaiseau Cedex, France. [14]Massachusetts Institute of Technology, Cambridge, MA 02139, USA. [15]School of Mathematics and Physics, Queen's University Belfast, University Rd, Belfast BT7 1NN, UK. [16]Max-Planck-Institut für Kernphysik, Postfach 10 39 80, 69029 Heidelberg, Germany. [17]Department of Physics, UNIST, Ulsan 689-798, Korea. [18]Los Alamos National Laboratory, Los Alamos, NM 87545, USA. [19]Rudolf Peierls Centre for Theoretical Physics, University of Oxford, Oxford OX1 3PU, UK. [20]Merton College, University of Oxford, Oxford OX1 4JD, UK.
*Corresponding author. Email: gianluca.gregori@physics.ox.ac.uk

Downloaded from https://www.science.org at University of York on August 29, 2024

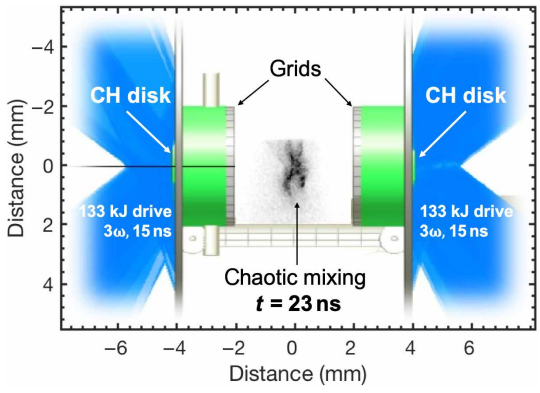

Fig. 1. Experimental configuration. Two polystyrene (CH) disks are separated by 8 mm and ablated with 96 frequency-tripled (351 nm wavelength) laser beams with a 1 mm spot diameter. The total laser illumination onto each disk is 133 ± 10 kJ in a 15 ns square pulse length. Turbulence is generated with plastic grid obstacles (300-μm aperture, 300-μm wires) located 2 mm away from each disk by disturbing both collimated flows before interpenetration and mixing. A gated x-ray detector (GXD) observes the chaotic mixing of the flows (shown here at 23 ns after the beginning of the laser drive), while proton radiography characterizes the self-generated magnetic fields. A 860-μm-diameter capsule, filled with 6 atm of D_2 gas and 12 atm of ^{3}He, is located 18 mm from the midpoint of the two disks and ablated with 60 frequency-tripled laser beams with a 200 μm spot that deliver 43 ± 5 kJ in a 900 ps square pulse length. The implosion produces 14.7-MeV monoenergetic protons that penetrate the interaction region and are collected by a CR-39 nuclear track detector. An optical Thomson scattering (OTS) probe of frequency-tripled light was focused to the midpoint between both disks, consisting of four beams, totaling 12.8 kJ in a 8 ns square pulse, to measure average electron density. In some shots, the OTS probe was swapped for a full-aperture backscatter system that measured the reflected light from four frequency-tripled lasers focused on the interaction region with 5.7 kJ in a 12.6 ns picket pulse and a 150 μm spot, to measure the turbulent velocity in the plasma.

turbulent velocity in the plasma was determined via stimulated Brillouin scattering (SBS). By recording the wavelength shift of the backscattered light from a probe beam, we infer $v_{\rm turb} \approx 200$ km/s. The self-generated magnetic fields were estimated from proton deflectometry to be $B_{\rm RMS} \approx 0.8 (B_{{\rm path},\parallel}/25{\rm kGcm})(\ell_B/100\mu{\rm m})^{1/2}(\ell_n/2{\rm mm})^{1/2}$ MG (here $B_{{\rm path},\parallel}$ is the one component of the magnetic field that we measure), where we took the proton path length ℓ_n from self-emission x-ray images (*19*, *20*), and the magnetic field correlation length, ℓ_B, corresponds to a wavelength $\sim 4\ell_B \approx 400$ μm of the same order as the grid periodicity. Using the same diagnostic, we found the maximum field to be $B_{\rm max} \gtrsim 3$ MG.

By comparing soft x-ray emission images in two wavelength bands determined by filtering the broadband emission with either 6.56-μm polyimide or 2.36-μm vanadium (see Fig. 2), two-dimensional maps of $\langle T_e \rangle_X$, a measure of the electron temperature averaged along the line of sight, were obtained with ~50-μm spatial resolution and ~100-ps temporal resolution (see the Supplementary Materials for details and validation with synthetic FLASH data). This temperature diagnostic closely resembles what has recently been used for galaxy-cluster x-ray analysis (*22*).

At $t \gtrsim 23$ ns after the start of the drive beams, we measured an average electron temperature measure $\langle T_e \rangle_X \approx 1.1$ keV over a 2 mm × 1 mm region: see Fig. 3. The profile of the $\langle T_e \rangle_X$ map is highly structured, with the magnitude of local perturbations in $\langle T_e \rangle_X$ exceeding ~500 eV through $t = 25$ ns.

Taking the measured root mean square (RMS) magnetic field, we find that the electrons in the interaction region are strongly magnetized (see the Supplementary Materials), viz., $r_g/\lambda_e \sim 0.08$, where r_g is their gyroradius and $\lambda_e \approx 0.1$ μm is their mean free path.

Note that $\lambda_e \lesssim \ell_T$, where $\ell_T \lesssim 50$ μm is the thermal gradient length scale (limited by the spatial resolution of the diagnostics), implies that ordinary (Spitzer) conductivity is somewhat modified by nonlocal effects (*23*). Nonlocal thermal conduction has been previously seen in laboratory experiments (*24*) and results in a smoothing of the heat front—increasing its width by a factor ~5 for $\lambda_e \sim \ell_T$ (*14*). However, in the presence of magnetic fields, electron conduction perpendicular to the field lines is further reduced by up to a factor $\sim \lambda_e/r_g$.

The parallel heat conduction is also quenched by a factor of $3/\beta_e$ (where β_e is the ratio of the electron thermal pressure to the magnetic pressure) due to the development of the whistler instability (*14*).

Evidence of notable reduction of heat conduction in our NIF experiment is illustrated by the electron temperature measure maps in Fig. 3. The image shows localized hot and cold patches with scale length $\ell_T \lesssim 50$ μm. For normal conduction, we should expect the time for the temperature gradients associated with the hot and cold spots to disappear to be $t_{\rm cond} \sim k_B n_e \ell_T^2/\kappa_S \sim 8 \times 10^{-12}$ s, where κ_S is the Spitzer thermal conductivity. Instead, as we do see temperature structures, they must have existed for a dynamical time $t_{\rm age} \sim L/c_s \sim 3 \times 10^{-9}$ s, where $L \sim 1$ mm is the spatial extent of the interaction region and c_s is the sound speed. This implies a reduction in the effective conductivity (κ) by a factor $(\kappa/\kappa_S)^{-1} \sim (t_{\rm age}/t_{\rm cond}) \gtrsim 100 - 200$ between $t = 23$ to 25 ns [see (*25*) for the same analysis applied to galaxy cluster plasmas].

DISCUSSION

The notion that the reduction in heat conduction is due to electrons being magnetized can be further strengthened if we compare NIF results with a turbulent plasma where $r_g/\lambda_e \gtrsim 1$, which was achieved in our previous experiments at the Omega laser facility, shown in Fig. 3C (*19*). While the turbulence itself exhibits a similar structure, the temperature map in this case is significantly more homogeneous, with $\ell_T \gg \lambda_e$, ℓ_B, and the same considerations as above lead to $(\kappa/\kappa_S)^{-1} \sim 1$, as expected for normal conduction.

Our analysis is supported by numerical simulations of the Omega and NIF experiments performed with the FLASH code. For both experiments, we generated x-ray images from the simulation outputs and synthetic temperature maps (Fig. 3, G to I; see the Supplementary Materials for details). For Omega, the code, run with Spitzer's conductivity, accurately reproduces the experimental $\langle T_e \rangle_X$ maps. For NIF, we compared simulation results for the cases when Spitzer thermal conduction was turned off to those with it included. We find that a highly structured $\langle T_e \rangle_X$ profile is only obtained in the conduction-off simulations.

More quantitatively, the distribution of $\langle T_e \rangle_X$ fluctuations in the interaction region agrees between the experimental data and synthetic predictions from the FLASH conduction-off simulations (Fig. 4A).

Although FLASH simulations lack the kinetic physics likely responsible for the suppression of conductivity in the experiment, this agreement is expected for the following reason. In the experiment, because thermal conductivity is suppressed, mixing of temperature perturbations by turbulent motions predominates over thermal diffusion for the smallest temperature fluctuations that are

Downloaded from https://www.science.org at University of York on August 29, 2024

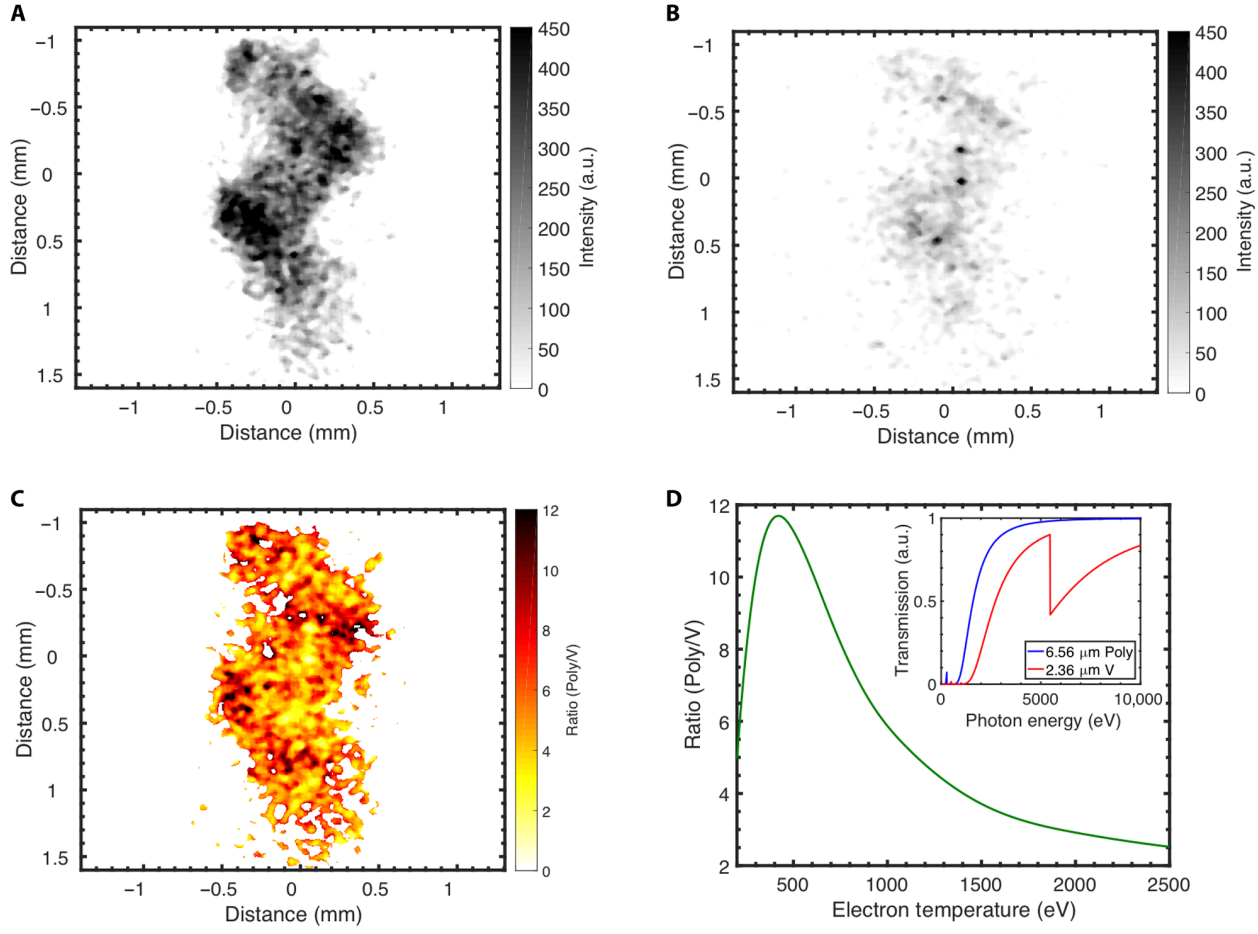

Fig. 2. X-ray emission images. A two-pinhole array coupled to a GXD camera was used to image simultaneously the plasma interaction region where turbulence was generated, with a different filter in front of each aperture. (**A**) Broadband x-ray emission filtered by 6.56-μm polyimide and (**B**) filtered by 2.36-μm vanadium foils at 25 ns after the initial drive lasers fired. The ratio of the x-ray emission in these two bands [polyimide/vanadium (Poly/V)] is shown in (**C**). In producing the image, regions within 20% of the background intensity were excluded, and a 50 μm (corresponding to the diameter of the pinholes) smoothing was applied. (**D**) Relation between the x-ray intensity ratio of polyimide to vanadium to the electron temperature of the plasma. The measured x-ray signal depends on the filter transmission (inset), the GXD camera response, and the plasma emission, which is a function of density and temperature. Since the wavelength dependence of the plasma emission is (mostly) insensitive to the density, the x-ray signal strengths from two different energy bands is a strong function of the temperature. When the temperature is larger than 450 eV, a one-to-one correspondence between the x-ray intensity ratio and the plasma temperature is thus obtained, in arbitrary units (a.u.).

resolved by our diagnostic. The conduction-off simulations have a similar resolution (25 μm) and a very small artificial viscosity (see the Supplementary Materials), so they capture the turbulent motions and the resulting temperature fluctuations on the same scales as the experimental diagnostic.

Evidence of substantial reduction of heat conduction in our NIF experiment is also supported by measurements made using an alternative copper-vanadium filter configuration that we compared with FLASH simulations (see the Supplementary Materials).

Further analysis of the simulations suggests a plausible candidate for the mechanism that gives rise to the temperature in homogeneities (that are then mixed by turbulent motions): A radiative cooling instability that acts on the initial temperature perturbations in the interaction region arising from asymmetries in the jets' collision. The instability is a result of line cooling due to the dopants in the plasma, which causes the cooling function for the plasma to be a strongly decreasing function of the temperature for much of the relevant range of temperatures (see the Supplementary Materials). As a result, regions in the simulated plasma where $T_e \lesssim 400$ eV and 700 eV $\lesssim T_e \lesssim$ 900 eV experience radiative cooling on a time scale that is comparable with the eddy turnover time of the turbulence (see Fig. 4B).

Also, approximate pressure balance across the whole interaction region (see the Supplementary Materials) implies that the regions that experience radiative cooling must undergo compression, while those that do not must expand (*26*, *27*), enhancing the impact of the cooling instability across the whole plasma. The instability cannot operate in the conduction-on simulations because the initial temperature fluctuations in the plasma are rapidly suppressed by efficient heat transport.

Our results provide the first direct experimental evidence of suppression of heat conduction in a turbulent magnetized plasma for conditions that resemble those of galaxy clusters, and, more generally, in high-β turbulent plasma with weakly collisional and magnetized electrons. They suggest that the effective electron conductivity is about two orders of magnitude below that predicted by Spitzer's

Downloaded from https://www.science.org at University of York on August 29, 2024

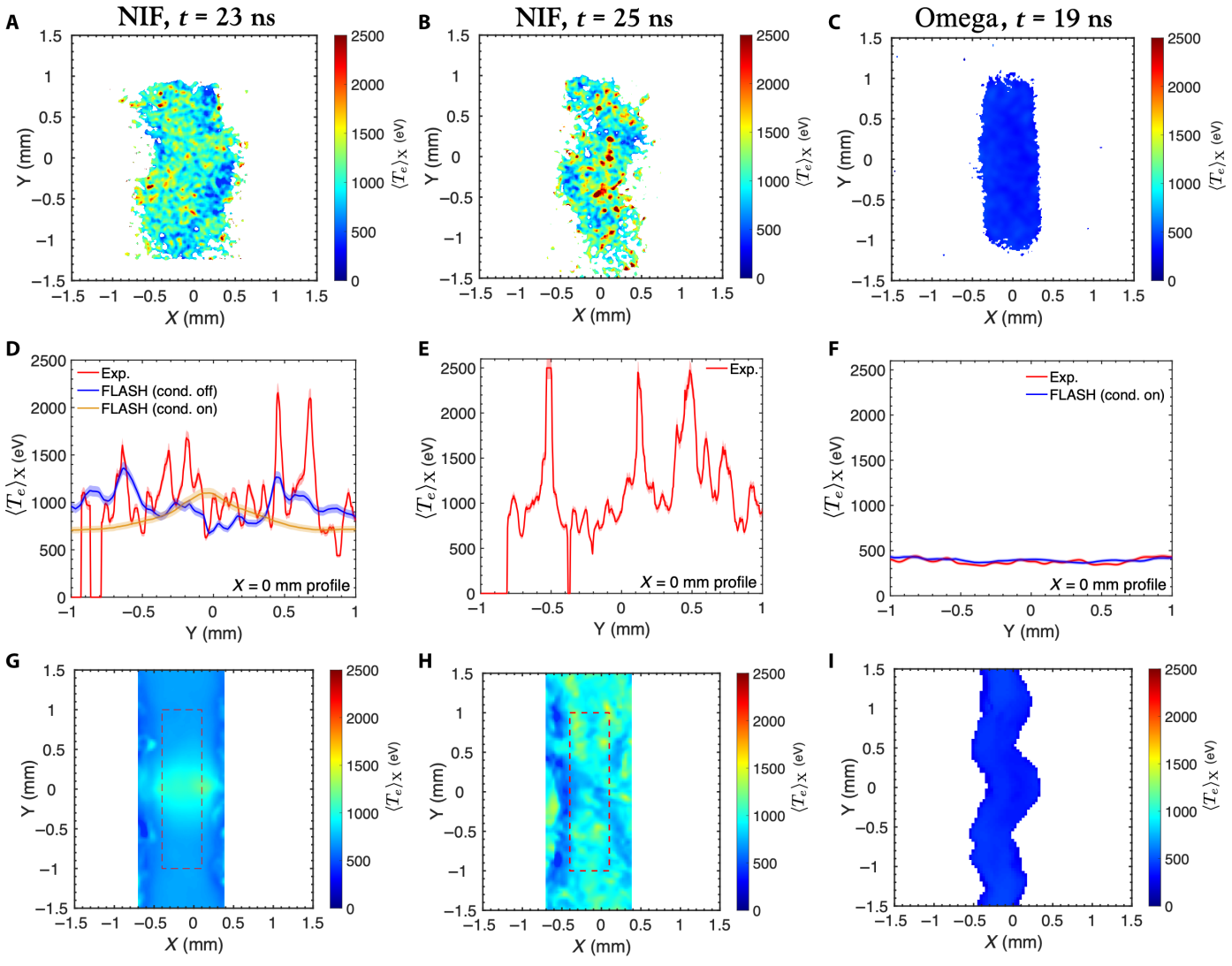

Fig. 3. Measured and simulated x-ray temperature maps. (**A**) Map of $\langle T_e \rangle_X$ at $t = 23$ ns after the start of the NIF laser drive. The maps are derived from the x-ray intensity ratio using the filter configuration described in Fig. 2. (**B**) Same as (A) but at $t = 25$ ns. (**C**) Same as (A), and for the same target as shown in Fig. 1, but driven using the Omega laser at 19 ns after the lasers fired. In this case, the $\langle T_e \rangle_X$ map was constructed by comparing x-ray measurements taken with a 50-μm pinhole camera filtered by 4-μm Mylar plus 80-nm Al and with 2-μm Mylar plus 40-nm Al (and assuming an average electron density of 10^{19} cm^{-3}). This diagnostic is sensitive to the temperature range 200 eV < $\langle T_e \rangle_X$ < 700 eV. Vertical $\langle T_e \rangle_X$ profiles taken at the $X = 0$ mm position for each of the previous maps in (A), (B), and (C) are shown in (**D**), (**E**), and (**F**), respectively, with a 5% error band added to each line. Equivalent $\langle T_e \rangle_X$ profiles from postprocessed FLASH simulations are also depicted. (**G**) Synthetic $\langle T_e \rangle_X$ map constructed by postprocessing FLASH simulation results of the NIF experiment (using the x-ray intensity ratio and GXD response as in the NIF experiment) at $t = 23$ ns. The map shown in this panel was obtained for the case of Spitzer thermal conduction switched on. (**H**) Same as (G) but with Spitzer thermal conduction switched off. (**I**) Same as (G) but for FLASH simulations of the Omega laser experiment at $t = 19$ ns, using the same x-ray intensity ratio and GXD response as in the Omega experiment and with Spitzer thermal conduction switched on.

theory, and so, e.g., in cluster cores, conduction is unlikely to be able to lower the AGN feedback requirements, which requires a conductivity larger than $\approx \kappa_S/5$ (*8*, *9*). Since both the experiment and the cluster plasma are in the regime where the electron Larmor radius is smaller than the mean free path, such strong modification in the heat transport points to plasma micro-instabilities as the main culprit for the reduction of classical Spitzer's conductivity (*14*, *15*). Precisely how to calculate the effective conductivity in such a plasma is currently unknown, either theoretically or numerically. Our NIF measurements thus provide an experimental benchmark for the development of future multiscale models of heat transport in turbulent and magnetized plasmas.

MATERIALS AND METHODS

OTS from collective electron plasma wave (EPW) oscillations was used to characterize the electron density in the interaction region of the two counterpropagating turbulent flows (*28*). Four laser beams were focused at the interaction region with a spot radius of 600 μm, forming a cylindrical collection volume of diameter 50 μm and length of 1.2 mm (see Fig. 1). From a scattering angle of 40°, light was collected by a spectrometer, dispersed by a grating, and streaked onto a camera to measure the temporal evolution of the electron density. The peak position of the EPW is mainly determined by the plasma frequency (via the plasma dispersion relation) (*28*). Since scattering occurs over a region that is much longer than the laser

Downloaded from https://www.science.org at University of York on August 29, 2024

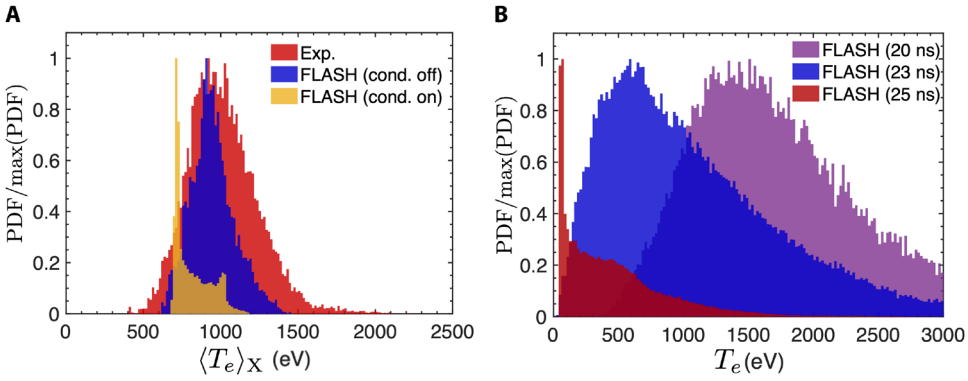

Fig. 4. Analysis of temperature fluctuations. (**A**) The normalized Probability Density Function (PDF) of $\langle T_e \rangle_X$ from the experimental data (see Fig. 3A) at t = 23 ns, compared with analogous distributions derived from the conduction-on and conduction-off FLASH simulations (see Fig. 3, G and H). In each case, the distribution is derived for an 0.5 mm by 2 mm area (demarcated by the red dashed lines in Fig. 3, G and H) and is normalized Probability Density Function (PDF) to its maximum value. (**B**) Distribution of actual temperatures in the conduction-off FLASH simulations in a 0.5 mm by 2 mm^2 volume centered on the interaction region at t = 20 ns (just after the jet collision), t = 23 ns and t = 25 ns. All points that are inside this volume butlie outside of the interaction region are excluded.

wavelength, in a turbulent plasma, this implies that different electron densities are probed simultaneously, and so the observed broadening of the EPW is a measurement of that range of densities.

Similar to OTS is the SBS diagnostic, which measures the light scattered back in the laser direction in a narrow wavelength range near the laser frequency. The SBS instability results from the resonant coupling between the probe laser light, the scattered light, and an ion-acoustic wave (*29*). To drive this instability, we use four NIF beams delivering 0.5 TW in a 100-μm spot, probing different points in the interaction region. The backscattered light (mostly occurring near the peak of the density profile) shows a frequency shift $\Delta\lambda_{SBS} = \Delta\lambda_{iaw} + \Delta\lambda_{flow}$, where $\Delta\lambda_{iaw}$ is associated with the coupling of the probe light with ion-acoustic waves, while $\Delta\lambda_{flow}$ is the Doppler contribution from the plasma flow moving in the direction of the laser beam. If the plasma temperature is known (from the temperature maps shown in Fig. 3), then $\Delta\lambda_{iaw}$ can be estimated, and the SBS diagnostic measures the component of the flow moving along the probe beam, which is nearly perpendicular to the axis connecting the two grids (see Fig. 1). Since the velocities near the center of the interaction region are chaotic (as confirmed by the FLASH simulations), the SBS measurement is indicative of the turbulent velocities achieved in the experiment.

The turbulence-amplified magnetic fields were inferred from the angular deflections of energetic protons as they traversed the interaction region. These were created by illuminating a D^3He capsule with 60 additional laser beams delivering a total of 48 kJ in a 900-ps pulse. Fusion reactions in the imploding capsule generate nearly monoenergetic 15-MeV protons. Unlike previous experiments where protons of these energies only acquired small deflections, proton deflections in the present experiment are large, with the trajectory of each individual proton crossing over those of other protons before reaching the detector. This prevents the application of previous analysis techniques capable of reconstructing two-dimensional maps of the path-integrated magnetic field (*30*).

To characterize the magnetic field, we instead measured the proton deflections by placing a slit in the path of the protons to limit the size of the beam as it entered the plasma. Qualitatively, the notable displacement of protons from their projected positions in the absence of any deflection is consistent with strong magnetic fields. More quantitatively, we measured the mean, the RMS, and the maximum displacement of the proton flux distribution from the slit's central position. This allows us to estimate the corresponding mean, RMS, and maximum values of the component of the path-integrated magnetic field parallel to the slit's orientation ($B_{path,\parallel} \equiv \int ds\, B_\parallel$). We also analyzed inhomogeneities in the proton flux distribution and found that their scale was consistent with the correlation length of the magnetic field being $\ell_B \approx 100$ μm. Further details of this analysis are provided in the Supplementary Materials.

SUPPLEMENTARY MATERIALS

Supplementary material for this article is available at https://science.org/doi/10.1126/sciadv.abj6799

REFERENCES AND NOTES

1. E. G. Zweibel, C. Heiles, Magnetic fields in galaxies and beyond. *Nature* **385**, 131–136 (1997).
2. V. Vacca, M. Murgia, F. Govoni, T. Enßlin, N. Oppermann, L. Feretti, G. Giovannini, F. Loi, Magnetic fields in galaxy clusters and in the large-scale structure of the Universe. *Galaxies* **6**, 142 (2018).
3. L. L. Cowie, J. Binney, Radiative regulation of gas flow within clusters of galaxies - A model for cluster x-ray sources. *Astrophys. J.* **215**, 723 (1977).
4. A. C. Fabian, Cooling flows in clusters of galaxies. *Annu. Rev. Astron. Astrophys.* **32**, 277–318 (1994).
5. A. Fabian, Observational evidence of active galactic nuclei feedback. *Annu. Rev. Astron. Astrophys.* **50**, 455–489 (2012).
6. L. Bîrzan, D. A. Rafferty, P. E. J. Nulsen, B. R. McNamara, H. J. A. Rottgering, M. W. Wise, R. Mittal, The duty cycle of radio-mode feedback in complete samples of clusters. *Mon. Not. R. Astron. Soc.* **427**, 3468–3488 (2012).
7. E. Churazov, W. Forman, C. Jones, H. Böhringer, Asymmetric, arc minute scale structures around NGC 1275. *Astron. Astrophys.* **356**, 788 (2000).
8. R. Narayan, M. V. Medvedev, Thermal conduction in clusters of Galaxies. *Astrophys. J.* **562**, L129–L132 (2001).
9. M. Ruszkowski, M. C. Begelman, Heating, conduction and minimum temperatures in cooling flows. *Astrophys. J.* **581**, 223–228 (2002).
10. M. W. Kunz, A. A. Schekochihin, S. C. Cowley, J. J. Binney, J. S. Sanders, Thermally stable heating mechanism for the intracluster medium: Turbulence, magnetic fields and plasma instabilities. *Mon. Not. R. Astron. Soc.* **410**, 2446–2457 (2011).
11. M. Markevitch, A. Vikhlinin, Shocks and cold fronts in galaxy clusters. *Phys. Rep.* **443**, 1–53 (2007).
12. S. V. Komarov, E. M. Churazov, M. W. Kunz, A. A. Schekochihin, Thermal conduction in a mirror-unstable plasma. *Mon. Not. R. Astron. Soc.* **460**, 467–477 (2016).
13. S. V. Komarov, E. M. Churazov, A. A. Schekochihin, J. A. ZuHone, Suppression of local heat flux in a turbulent magnetized intracluster medium. *Mon. Not. R. Astron. Soc.* **440**, 1153–1164 (2014).

Downloaded from https://www.science.org at University of York on August 29, 2024

14. S. Komarov, A. A. Schekochihin, E. Churazov, A. Spitkovsky, Self-inhibiting thermal conduction in a high-β, whistler-unstable plasma. *J. Plasma Phys.* **84**, 905840305 (2018).
15. G. T. Roberg-Clark, J. F. Drake, C. S. Reynolds, M. Swisdak, Suppression of electron thermal conduction by whistler turbulence in a sustained thermal gradient. *Phys. Rev. Lett.* **120**, 035101 (2018).
16. J. A. ZuHone, M. Markevitch, M. Ruszkowski, D. Lee, Cold fronts and gas sloshing in galaxy clusters with anisotropic thermal conduction. *Astrophys. J.* **762**, 69 (2013).
17. B. Smith, B. W. O'Shea, G. M. Voit, D. Ventimiglia, S. W. Skillman, Cosmological simulations of isotropic conduction in galaxy clusters. *Astrophys. J.* **778**, 152 (2013).
18. G. Gregori, B. Reville, F. Miniati, The generation and amplification of intergalactic magnetic fields in analogue laboratory experiments with high power lasers. *Phys. Rep.* **601**, 1–34 (2015).
19. P. Tzeferacos, A. Rigby, A. F. A. Bott, A. R. Bell, R. Bingham, A. Casner, F. Cattaneo, E. M. Churazov, J. Emig, F. Fiuza, C. B. Forest, J. Foster, C. Graziani, J. Katz, M. Koenig, C. K. Li, J. Meinecke, R. Petrasso, H. S. Park, B. A. Remington, J. S. Ross, D. Ryu, D. Ryutov, T. G. White, B. Reville, F. Miniati, A. A. Schekochihin, D. Q. Lamb, D. H. Froula, G. Gregori, Laboratory evidence of dynamo amplification of magnetic fields in a turbulent plasma. *Nat. Commun.* **9**, 591 (2018).
20. A. F. A. Bott, P. Tzeferacos, L. Chen, C. A. J. Palmer, A. Rigby, A. R. Bell, R. Bingham, A. Birkel, C. Graziani, D. H. Froula, J. Katz, M. Koenig, M. W. Kunz, C. Li, J. Meinecke, F. Miniati, R. Petrasso, H. S. Park, B. A. Remington, B. Reville, J. S. Ross, D. Ryu, D. Ryutov, F. H. Séguin, T. G. White, A. A. Schekochihin, D. Q. Lamb, G. Gregori, Time-resolved turbulent dynamo in a laser plasma. *Proc. Natl. Acad. Sci.* **118**, e2015729118 (2021).
21. P. Tzeferacos, A. Rigby, A. Bott, A. R. Bell, R. Bingham, A. Casner, F. Cattaneo, E. M. Churazov, J. Emig, N. Flocke, F. Fiuza, C. B. Forest, J. Foster, C. Graziani, J. Katz, M. Koenig, C. K. Li, J. Meinecke, R. Petrasso, H. S. Park, B. A. Remington, J. S. Ross, D. Ryu, D. Ryutov, K. Weide, T. G. White, B. Reville, F. Miniati, A. A. Schekochihin, D. H. Froula, G. Gregori, D. Q. Lamb, Numerical modeling of laser-driven experiments aiming to demonstrate magnetic field amplification via turbulent dynamo. *Phys. Plasmas* **24**, 041404 (2017).
22. E. Churazov, P. Arevalo, W. Forman, C. Jones, A. Schekochihin, A. Vikhlinin, I. Zhuravleva, Arithmetic with x-ray images of galaxy clusters: Effective equation of state for small-scale perturbations in the ICM. *Mon. Not. R. Astron. Soc.* **463**, 1057–1067 (2016).
23. A. R. Bell, R. G. Evans, D. J. Nicholas, Elecron energy transport in steep temperature gradients in laser-produced plasmas. *Phys. Rev. Lett.* **46**, 243–246 (1981).
24. G. Gregori, S. H. Glenzer, J. Knight, C. Niemann, D. Price, D. H. Froula, M. J. Edwards, R. P. J. Town, A. Brantov, W. Rozmus, V. Y. Bychenkov, Effect of nonlocal transport on heat-wave propagation. *Phys. Rev. Lett.* **92**, 205006 (2004).
25. M. Markevitch, P. Mazzotta, A. Vikhlinin, D. Burke, Y. Butt, L. David, H. Donnelly, W. R. Forman, D. Harris, D. W. Kim, S. Virani, J. Vrtilek, [ITAL]Chandra[/ITAL] temperature map of A754 and constraints on thermal conduction. *Astrophys. J.* **586**, L19–L23 (2003).
26. D. A. Tidman, R. A. Shanny, Field-generating thermal instability in laser-heated plasmas. *Phys. Fluids* **17**, 1207 (1974).
27. M. G. Haines, Thermal instability and magnetic field generated by large heat flow in a plasma, especially under laser-fusion conditions. *Phys. Rev. Lett.* **47**, 917–920 (1981).
28. D. E. Evans, J. Katzenstein, Laser light scattering in laboratory plasmas. *Rep. Prog. Phys.* **32**, 207–271 (1969).
29. H. A. Rose, D. F. DuBois, Laser hot spots and the breakdown of linear instability theory with application to stimulated Brillouin scattering. *Phys. Rev. Lett.* **72**, 2883–2886 (1994).
30. A. Bott, C. Graziani, P. Tzeferacos, T. G. White, D. Q. Lamb, G. Gregori, A. A. Schekochihin, Proton imaging of stochastic magnetic fields. *J. Plasma Phys.* **83**, 905830614 (2017).
31. G. A. Rochau, J. E. Bailey, G. A. Chandler, T. J. Nash, D. S. Nielsen, G. S. Dunham, O. F. Garcia, N. R. Joseph, J. W. Keister, M. J. Madlener, D. B. Morgan, K. J. Moy, M. Wu, Energy dependent sensitivity of microchannel plate detectors. *Rev. Sci. Instrum.* **77**, 10E323 (2006).
32. B. A. Fryxell, K. Olson, P. Ricker, F. X. Timmes, M. Zingale, D. Q. Lamb, P. M. Neice, R. Rosner, J. W. Truran, H. Tufo, FLASH: An adaptive mesh hydrodynamics code for modeling astrophysical thermonuclear flashes. *Astrophys. J. Suppl.* **131**, 273–334 (2000).
33. D. Lee, A solution accurate, efficient and stable unsplit staggered mesh scheme for three dimensional magnetohydrodynamics. *J. Comput. Phys.* **243**, 269–292 (2013).
34. P. Tzeferacos, M. Fatenejad, N. Flocke, C. Graziani, G. Gregori, D. Q. Lamb, D. Lee, J. Meinecke, A. Scopatz, K. Weide, FLASH MHD simulations of experiments that study shock-generated magnetic fields. *High Energ. Dens. Phys.* **17**, 24–31 (2015).
35. S. I. Braginskii, Transport processes in a plasma. *Rev. Plasma Phys.* **1**, 205 (1965).
36. M. Fatenejad, B. Fryxell, J. Wohlbier, E. Myra, D. Lamb, C. Fryer, C. Graziani, Collaborative comparison of simulation codes for high-energy-density physics applications. *High Energ. Dens. Phys.* **9**, 63–66 (2013).
37. C. Orban, M. Fatenejad, S. Chawla, S. C. Wilks, D. Q. Lamb, A radiation-hydrodynamics code comparison for laser-produced plasmas: FLASH versus HYDRA and the results of validation experiments (2013); arXiv preprint arXiv:1306.1584.
38. J. Meinecke, H. W. Doyle, F. Miniati, A. R. Bell, R. Bingham, R. Crowston, R. P. Drake, M. Fatenejad, M. Koenig, Y. Kuramitsu, C. C. Kuranz, D. Q. Lamb, D. Lee, M. J. MacDonald, C. D. Murphy, H. S. Park, A. Pelka, A. Ravasio, Y. Sakawa, A. A. Schekochihin, A. Scopatz, P. Tzeferacos, W. C. Wan, N. C. Woolsey, R. Yurchak, B. Reville, G. Gregori, Turbulent amplification of magnetic fields in laboratory laser-produced shock waves. *Nat. Phys.* **10**, 520–524 (2014).
39. K. Falk, E. J. Gamboa, G. Kagan, D. S. Montgomery, B. Srinivasan, P. Tzeferacos, J. F. Benage, Equation of state measurements of warm dense carbon using laser-driven shock and release technique. *Phys. Rev. Lett.* **112**, 155003 (2014).
40. R. Yurchak, A. Ravasio, A. Pelka, S. Pikuz, E. Falize, T. Vinci, M. Koenig, B. Loupias, A. Benuzzi-Mounaix, M. Fatenejad, P. Tzeferacos, D. Q. Lamb, E. G. Blackman, Experimental demonstration of an inertial collimation mechanism in nested outflows. *Phys. Rev. Lett.* **112**, 155001 (2014).
41. C. K. Li, P. Tzeferacos, D. Lamb, G. Gregori, P. A. Norreys, M. J. Rosenberg, R. K. Follett, D. H. Froula, M. Koenig, F. H. Seguin, J. A. Frenje, H. G. Rinderknecht, H. Sio, A. B. Zylstra, R. D. Petrasso, P. A. Amendt, H. S. Park, B. A. Remington, D. D. Ryutov, S. C. Wilks, R. Betti, A. Frank, S. X. Hu, T. C. Sangster, P. Hartigan, R. P. Drake, C. C. Kuranz, S. V. Lebedev, N. C. Woolsey, Scaled laboratory experiments explain the kink behaviour of the crab nebula jet. *Nat. Commun.* **7**, 13081 (2016).
42. A. Rigby, F. Cruz, B. Albertazzi, R. Bamford, A. R. Bell, J. E. Cross, F. Fraschetti, P. Graham, Y. Hara, P. M. Kozlowski, Y. Kuramitsu, D. Q. Lamb, S. Lebedev, J. R. Marques, F. Miniati, T. Morita, M. Oliver, B. Reville, Y. Sakawa, S. Sarkar, C. Spindloe, R. Trines, P. Tzeferacos, L. O. Silva, R. Bingham, M. Koenig, G. Gregori, Electron acceleration by wave turbulence in a magnetized plasma. *Nat. Phys.* **14**, 475–479 (2018).
43. Y. Lu, P. Tzeferacos, E. Liang, R. K. Follett, L. Gao, A. Birkel, D. H. Froula, W. Fu, H. Ji, D. Lamb, C. K. Li, H. Sio, R. Petrasso, M. S. Wei, Numerical simulation of magnetized jet creation using a hollow ring of laser beams. *Phys. Plasmas* **26**, 022902 (2019).
44. L. Gao, E. Liang, Y. Lu, R. K. Follet, H. Sio, P. Tzeferacos, D. H. Froula, A. Birkel, C. K. Li, D. Lamb, R. Petrasso, W. Fu, M. Wei, H. Ji, Mega-gauss plasma jet creation using a ring of laser beams. *Astrophys. J.* **873**, L11 (2019).
45. T. G. White, M. T. Oliver, P. Mabey, M. Kühn-Kauffeldt, A. F. A. Bott, L. N. K. Döhl, A. R. Bell, R. Bingham, R. Clarke, J. Foster, G. Giacinti, P. Graham, R. Heathcote, M. Koenig, Y. Kuramitsu, D. Q. Lamb, J. Meinecke, T. Michel, F. Miniati, M. Notley, B. Reville, D. Ryu, S. Sarkar, Y. Sakawa, M. P. Selwood, J. Squire, R. H. H. Scott, P. Tzeferacos, N. Woolsey, A. A. Schekochihin, G. Gregori, Supersonic plasma turbulence in the laboratory. *Nat. Commun.* **10**, 1758 (2019).
46. L. E. Chen, A. F. A. Bott, P. Tzeferacos, A. Rigby, A. Bell, R. Bingham, C. Graziani, J. Katz, M. Koenig, C. K. Li, R. Petrasso, H. S. Park, J. S. Ross, D. Ryu, T. G. White, B. Reville, J. Matthews, J. Meinecke, F. Miniati, E. G. Zweibel, S. Sarkar, A. A. Schekochihin, D. Q. Lamb, D. H. Froula, G. Gregori, Transport of high-energy charged particles through spatially intermittent turbulent magnetic fields. *Astrophys. J.* **892**, 114 (2020).
47. A. F. A. Bott, L. Chen, G. Boutoux, T. Caillaud, A. Duval, M. Koenig, B. Khiar, I. Lantuéjoul, L. le-Deroff, B. Reville, R. Rosch, D. Ryu, C. Spindloe, B. Vauzour, B. Villette, A. A. Schekochihin, D. Q. Lamb, P. Tzeferacos, G. Gregori, A. Casner, Inefficient magnetic-field amplification in supersonic laser-plasma turbulence. *Phys. Rev. Lett.* **127**, 175002 (2021).
48. S. A. Muller, D. N. Kaczala, H. M. Abu-Shawareb, E. L. Alfonso, L. C. Carlson, M. Mauldin, P. Fitzsimmons, D. Lamb, P. Tzeferacos, L. Chen, G. Gregori, A. Rigby, A. Bott, T. G. White, D. Froula, J. Katz, Evolution of the design and fabrication of astrophysics targets for turbulent dynamo (tdyno) experiments on omega. *Fusion Sci. Technol.* **73**, 434–445 (2018).
49. P. Colella, P. R. Woodward, The piecewise parabolic method (ppm) for gas-dynamical simulations. *J. Comput. Phys.* **54**, 174–201 (1984).

Acknowledgments

Funding: The research leading to these results received funding from the U.K. EPSRC (grant numbers EP/M022331/1 and EP/N014472/1); the European Research Council under the European Community's Seventh Framework Programme (FP7/2007-2013)/ERC grant agreements nos. 256973 and 247039; the U.S. DOE under Contract No. B591485 to LLNL; Field Work Proposal No. 57789 to ANL and DE-SC0016566, DE-NA0003605, and DE-NA0003934 to the University of Chicago; DE-NA0003868 to the Massachusetts Institute of Technology; DE-NA0001808, 89233118CNA000010, and 89233119CNA000063 to General Atomics; subcontract nos. 536203 and 630138 (LANL) and B632670 (LLNL) to the Flash Center for Computational Science; and Cooperative Agreement DE-NA0003856 to the Laboratory for Laser Energetics (LLE), University of Rochester. LLNL work was performed under the auspices of the U.S. Department of Energy by Lawrence Livermore National Laboratory under Contract DE-AC52-07NA27344. We acknowledge support from the NSF under grants PHY-1619573 and PHY-2033925. Awards of compute time were provided by the U.S. DOE ALCC program. Compute time was provided by the U.S. DOE ALCC and ERCAP programs, and the LLE High Performance Computing group. We acknowledge funding from grants 2016R1A5A1013277 and 2020R1A2C2102800 of the NRF of Korea. The work of AAS was supported in part by the

Downloaded from https://www.science.org at University of York on August 29, 2024

U.K. EPSRC Programme Grant EP/R034737/1. Support from AWE plc. and the STFC of the U.K. is also acknowledged. The NIF shots were allocated through the NIF Discovery Science Program. The software used in this work was developed in part by the DOE NNSA- and DOE Office of Science-supported Flash Center for Computational Science at the University of Chicago and the University of Rochester. **Author contributions:** G.G., J.S.R., A.F.A.B., P.T., A.A.S., F.M., and D.Q.L. conceived the project, with G.G. leading the experimental program. J.M. and J.S.R. coordinated the shots on NIF; J.M. and J.F. developed the x-ray temperature diagnostics and J.M. performed the data analysis; B.L., C.-K.L., R.P., and A.F.A.B. contributed to the proton radiography development and data extraction; J.S.R. and J.M. contributed to the Thomson scattering diagnostics; P.T. designed, executed, and analyzed the FLASH simulations; J.M. and A.F.A.B. led the analysis of the experimental and simulation data, with support from P.T., S.F., H.-S.P., A.R.B., R.Bl., R.Bi., R.L.B., A.C., L.E.C., D.H.F., C.G., D.K., M.K., Y.L., C.A.J.P., H.P., B.Rem., B.Rev., A.Re., A.Ri., D.R., G.S., A.Z., F.M., S.S., A.A.S., D.Q.L., and G.G.; and J.M. and G.G. wrote the paper with contribution from all co-authors. **Competing interests:** D.Q.L. received consulting fees from Lawrence Livermore National Laboratory. All other authors declare that they have no competing interests. **Data and materials availability:** All data needed to evaluate the conclusions in the paper are present in the paper and/or the Supplementary Materials. All the data shown in the paper's figures have been deposited in Oxford University Research Archive (ORA)–data (https://ora.ox.ac.uk/objects/uuid:fb17fe8d-fd07-444e-aa7e-e8b021fa463e). All other data are available in the main text or the Supplementary Materials. The FLASH code is publicly available at https://flash.rochester.edu.

Submitted 25 May 2021
Accepted 19 January 2022
Published 9 March 2022
10.1126/sciadv.abj6799

Downloaded from https://www.science.org at University of York on August 29, 2024